

STRUCTURE FUNCTIONS AND LARGE Q^2 CROSS SECTIONS AT HERA

Giuseppe Iacobucci *

INFN-Sezione di Bologna, Via Irnerio 46, I-40126 Bologna, Italy

Abstract

The data collected with the H1 and ZEUS detectors during the running period 1994-99 are used to give an experimental review on the proton structure functions and the neutral current and charged current large Q^2 cross sections in $e^\pm p$ scattering at HERA.

* Talk given on behalf of the H1 and ZEUS collaborations at the Workshop on Results and Perspectives in Particle Physics, La Thuile, Italy, February 2000

1 Foreword

With the advent of the HERA $e^\pm p$ collider at DESY, enormous progress in the measurement of the proton structure has been made. The large HERA ep centre-of-mass energy $\sqrt{s} = 300 - 318$ GeV, obtained with a lepton-beam energy $E_e = 27.5$ GeV and proton-beam energies $E_p = 820$ GeV until 1997 and $E_p = 920$ GeV since 1998, allowed the two collider experiments H1 and ZEUS to measure F_2 up to virtualities of the exchanged boson $Q^2 \sim 10^5$ GeV 2 and down to Bjorken $x \sim 10^{-6}$. These measurements constitute an extension by more than two orders of magnitude of the (x, Q^2) range in which we have knowledge of the proton structure (see Fig. 1). The study of $e^\pm p$ interactions is important throughout the above kinematic range,

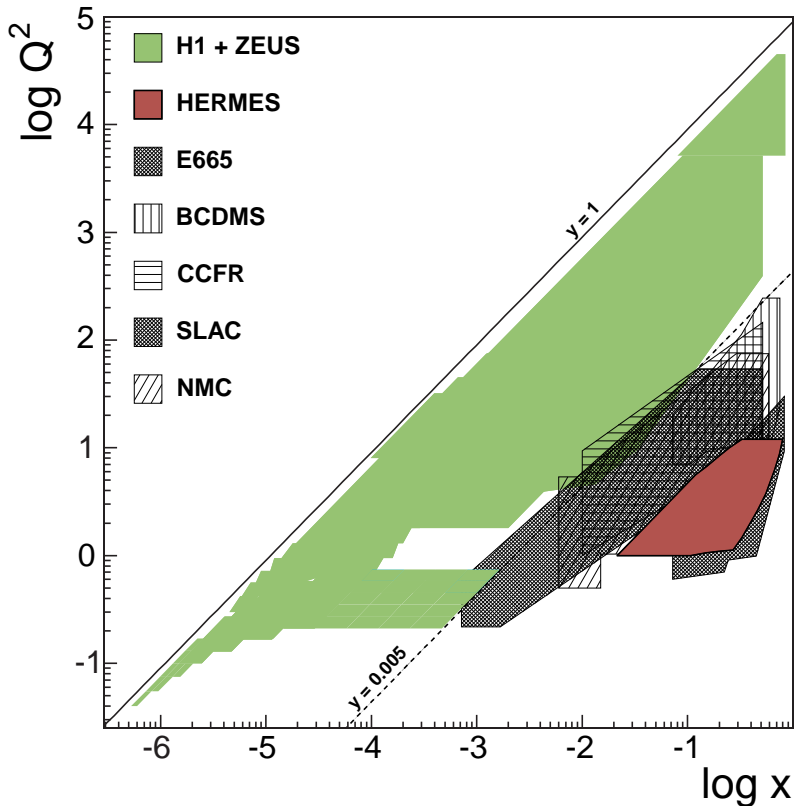


Figure 1: The (x, Q^2) kinematic plane, showing the range covered by the HERA and the fixed target measurements.

not only because of the structure functions, which allow a calculation of the expected rates at the LHC and an estimation of the νN cross sections for ultra-high-energy neutrinos ¹⁾ ($E_\nu \sim 10^{12}$ GeV) from active galactic nuclei and γ -ray bursts, but also because of several theoretical issues still open in this field:

- it is of primary importance to study the transition from the photoproduction ($Q^2 \sim 0$) to the deep inelastic scattering (DIS, $Q^2 \gtrsim \text{few GeV}^2$) regime to see at which value of Q^2 perturbative QCD (pQCD) begins to dominate ²⁾;
- the strong rise of F_2 measured in DIS at HERA for $x \rightarrow 0$ is a well established and important fact. However, it is imperative to measure F_2 with higher and higher precision over a wide kinematic range, in order to address the issues of parton saturation at very small x ³⁾ and QCD evolution (the BFKL evolution ⁴⁾, which ought to be important when terms in $\ln \frac{1}{x}$ become large, has yet to be observed experimentally);
- as will be shown in the following, the study of electroweak (EW) physics at HERA ⁵⁾ is just beginning. Large luminosities both with electrons and positrons, as well as polarised beams, are needed to perform these studies, which have always been one of the main aims of HERA;
- the exploration of new kinematic regimes may reveal new physics. The breakdown of the Standard Model may manifest itself as deviations of the measured cross sections from the predictions at very large (x, Q^2).

In this document, an experimental review will be given of the knowledge of proton structure functions and ep cross sections at large Q^2 using the H1 and ZEUS results, obtained with the $\sim 70 \text{ pb}^{-1}$ of e^+p and $\sim 15 \text{ pb}^{-1}$ of e^-p collisions that each experiment has collected until the end of 1999.

2 Kinematics

In inclusive deep inelastic scattering, $e(k) + p(P) \rightarrow e(k') + X$, the proton structure functions are expressed in terms of the negative of the four-momentum transfer squared:

$$Q^2 = -q^2 = -(k - k')^2$$

and of the Bjorken x :

$$x = \frac{Q^2}{2P \cdot q}$$

where k and P are the four-momenta of the incoming particles and k' is the four-momentum of the scattered lepton. The fraction of the lepton energy transferred to the proton in its rest frame is $y = Q^2/(sx)$. The ZEUS and H1 detectors measure the energies and angles of the scattered lepton and hadronic system. These four independent quantities over-constrain the kinematic variables x and Q^2 (or, equivalently, y and Q^2). In order to optimise the reconstruction of the kinematic variables,

the two collaborations use different methods, dictated by the characteristics of their detectors ²⁾.

3 The proton structure functions

In inclusive deep inelastic scattering the double differential cross section for the exchange of a neutral current (NC) is given by:

$$\frac{d^2\sigma_{NC}^{e^\pm p}}{dx dQ^2} = \frac{2\pi\alpha^2}{xQ^4} [Y_+ F_2(x, Q^2) - y^2 F_L(x, Q^2) \mp Y_- x F_3(x, Q^2)] (1 + \delta_r(x, Q^2)) \quad (1)$$

where $Y_\pm = 1 \pm (1-y)^2$, α is the EW coupling constant and δ_r is the EW radiative correction. In leading order QCD and for longitudinally unpolarized beams, the longitudinal structure function $F_L = 0$, while the structure functions F_2 and $x F_3$ are expressed as sums over the quark flavor f of the product of the EW quark couplings, A_f and B_f , and the quark momentum distributions in the proton $q_f(x, Q^2)$:

$$F_2 = x \sum_f A_f^2 \cdot (q_f(x, Q^2) + \bar{q}_f(x, Q^2))$$

$$xF_3 = x \sum_f B_f^2 \cdot (q_f(x, Q^2) - \bar{q}_f(x, Q^2))$$

where, at low Q^2 , A_f reduces to the quark electric charge. The parity violating term $x F_3$, due to Z^0 exchange, becomes relevant only for $Q^2 \simeq M_{Z^0}^2$, where M_{Z^0} is the mass of the Z^0 boson. Beyond the leading order in QCD, the emission of gluons allows longitudinally polarised photons to be absorbed by spin $\frac{1}{2}$ quarks. Therefore F_L becomes non-zero and can be written as a function of F_2 and the gluon momentum distribution $xg(x, Q^2)$:

$$F_L = \frac{\alpha_s}{4\pi} x^2 \int \frac{dz}{z^3} \left[\frac{16}{3} F_2 + 8 \sum_i e_i^2 \left(1 - \frac{x}{z} \right) z g \right]. \quad (2)$$

The effect of F_L on the cross section is negligible at small values of y and becomes substantial at large y .

3.1 High precision F_2 measurements at very small (x, Q^2)

During 1997, the beam pipe tracker ⁶⁾ (BPT), a tracking device based on silicon microstrip technology, was installed in the ZEUS detector in front of the existing beam pipe calorimeter (BPC), a small electromagnetic sampling calorimeter positioned at small scattered-lepton angles to measure the energy of the scattered lepton in low- Q^2 events. The installation of the BPT improved the measurement of the

ZEUS 1997

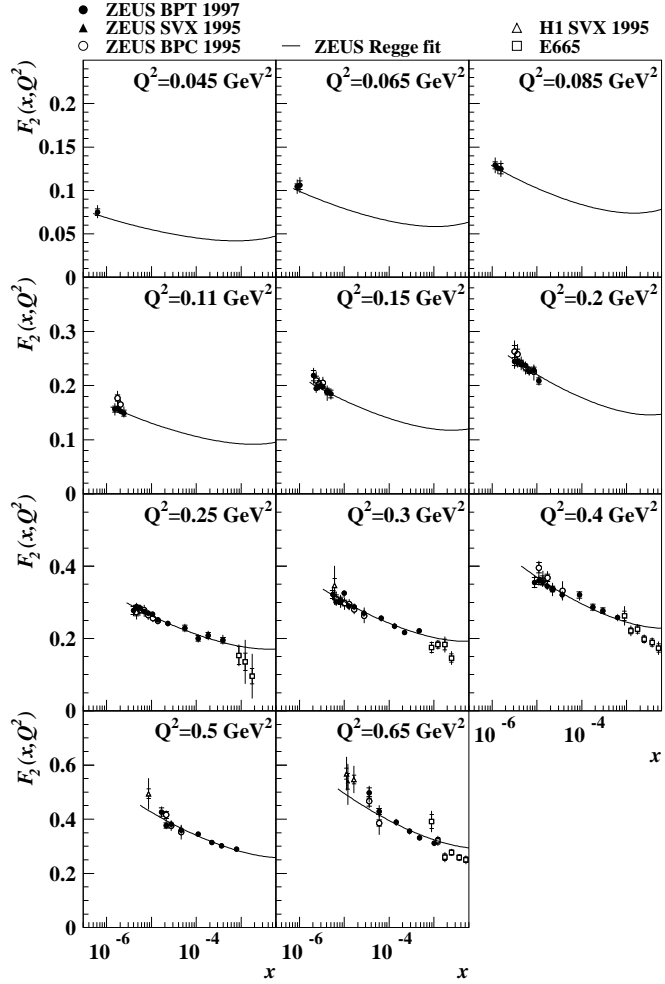


Figure 2: The HERA measurement of F_2 at very small x and Q^2 . E665 data are also shown. The lines are the result of a fit to the data based on Regge phenomenology⁶⁾.

scattered-lepton angle and allowed the fiducial range of the BPC to be increased, thus extending the kinematic range of the F_2 measurement at very small (x, Q^2) to $0.045 < Q^2 < 0.65 \text{ GeV}^2$ and $6 \cdot 10^{-7} < x < 1 \cdot 10^{-3}$. The measured F_2 as a function of x for several Q^2 values, obtained with 3.9 pb^{-1} of e^+p collisions collected with the BPT, are shown in Fig. 2. The typical uncertainties are $\pm 2.6\%(\text{stat.})$ and $\pm 3.3\%(\text{syst.})$. The rise of F_2 for $x \rightarrow 0$ is measured to become slower as Q^2 decreases, and can be described by Regge theory with a constant logarithmic slope. The dependence of F_2 on Q^2 is stronger than at higher Q^2 values, approaching, at the lowest Q^2 of this measurement, a region where F_2 becomes nearly proportional to Q^2 ⁶⁾.

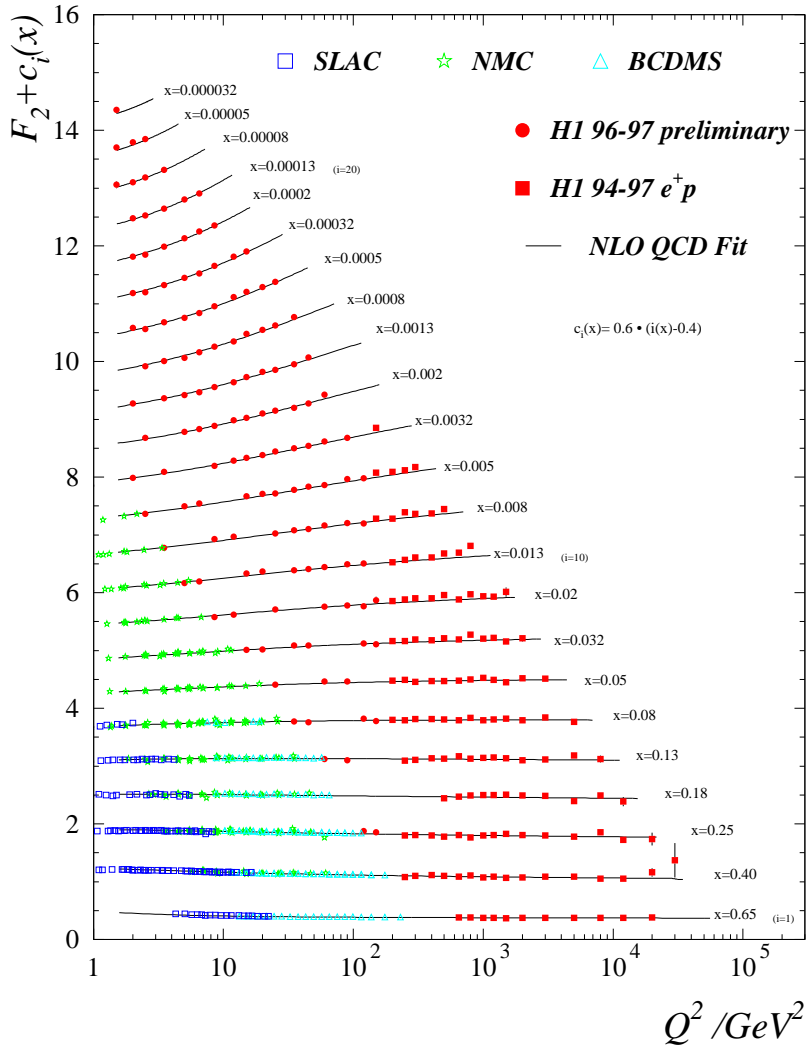


Figure 3: The H1 measurement of F_2 vs. Q^2 in bins of x ; fixed-target data and the $H1$ $pQCD$ NLO fit are also shown. In order to improve visibility, the data and the fit are multiplied by the $c_i(x)$ factors as shown in the Figure.

3.2 F_2 , its derivatives and the QCD NLO fit at medium Q^2

3.2.1 F_2 measurements at medium Q^2 at HERA: precision data

The data samples collected during 1996-97 with the H1 and ZEUS detectors, each corresponding to approximately 40 pb^{-1} , made possible a precise measurement of F_2 at medium Q^2 . This improvement was possible both because of the higher statistics and a better knowledge of the systematic uncertainties. The latter was partly due to the installation of new detector components, such as the H1 backward silicon detector. Typical uncertainties of approximately 1% statistical and 2 – 3% systematic were achieved, thus approaching the precision of the fixed-target experi-

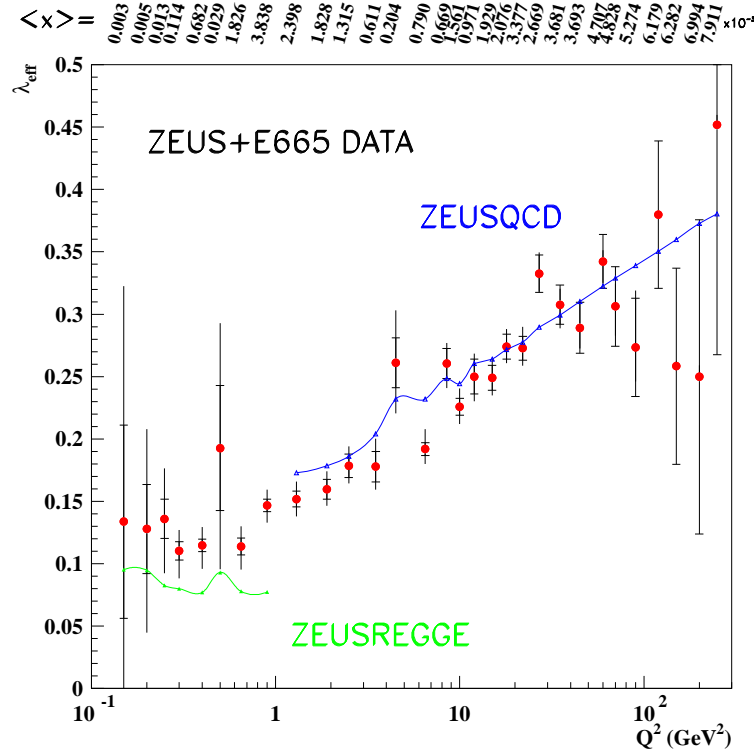


Figure 4: The derivative $d \ln F_2 / d \ln \frac{1}{x} = \lambda_{\text{eff}}$ as a function of Q^2 calculated by fitting $F_2 = Ax^{-\lambda_{\text{eff}}}$ to the E665 and ZEUS data with $x < 0.01$. The ZEUSREGGE and ZEUSQCD calculations are from the Regge and NLO QCD fits¹³⁾. The average x values of the various points are reported on the top of the Figure.

ments. An overview of the F_2 measurements^{7, 8)} is given in Fig. 3. The HERA and the fixed-target data agree in the region of overlap. A pQCD next-to-leading-order (NLO) fit (see Section 3.2.3) using the DGLAP evolution equations⁹⁾ describes the data over the full range of the measurement. Scaling violations are well described by the fit. There is no indication that the HERA data require any $(\ln \frac{1}{x})^n$ BFKL-type correction terms to the standard DGLAP evolution.

3.2.2 Derivatives of F_2

As pointed out in the literature¹⁰⁾, the slopes $d \ln F_2 / d \ln \frac{1}{x}$ and $dF_2 / d \ln Q^2$ contain a lot of information. At fixed Q^2 and at small x the behaviour of F_2 can be characterised by $F_2 \propto x^{-\lambda_{\text{eff}}}$, so that $\lambda_{\text{eff}} = d \ln F_2 / d \ln \frac{1}{x}$. The value of λ_{eff} as an observable at small x has been discussed by Navelet et al.^{11, 12)}. The E665 and ZEUS F_2 data at fixed Q^2 and $x < 0.01$ have been fitted to the form $Ax^{-\lambda_{\text{eff}}}$ ¹³⁾. Fig. 4 shows the measured values of λ_{eff} as a function of Q^2 . Regge phenomenology

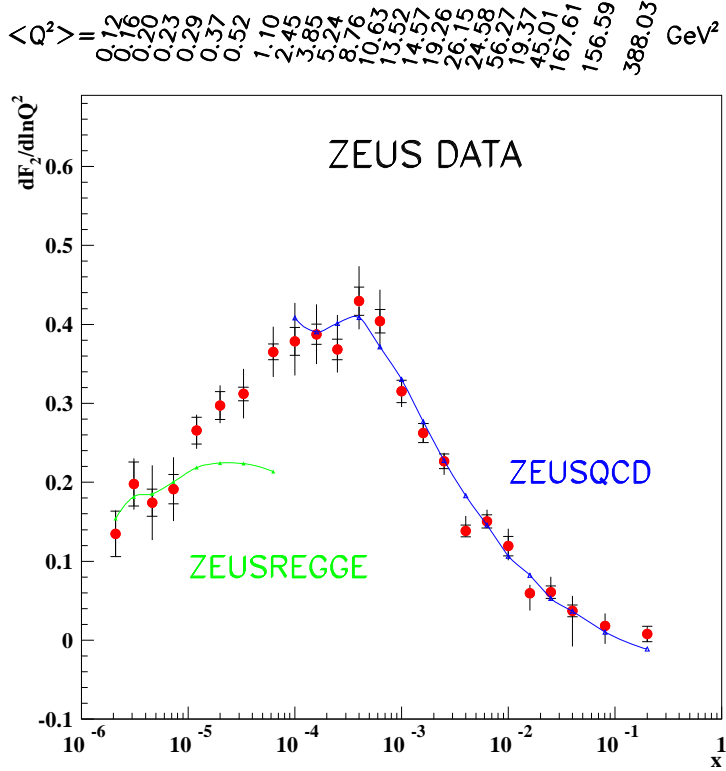


Figure 5: The derivative $dF_2/d \ln Q^2$ as a function of x calculated by fitting ZEUS F_2 data in bins of x to the form $a + b \ln Q^2$. The ZEUSREGGE and ZEUSQCD calculations are from the Regge and NLO QCD fits¹³⁾. The average Q^2 of the various points is shown on the top of the Figure.

predicts $\lambda_{eff} = \alpha_P(0) - 1 \approx 0.1$ independent of Q^2 , where $\alpha_P(0)$ is the intercept of the pomeron trajectory. Data for $Q^2 < 1 \text{ GeV}^2$ are consistent with this prediction. For $Q^2 > 1 \text{ GeV}^2$, λ_{eff} is observed to rise, reaching approximately 0.3 at $Q^2 = 50 \text{ GeV}^2$. The rise of λ_{eff} with Q^2 is described by pQCD¹²⁾, in particular by the ZEUS pQCD NLO fit, based on DGLAP evolution equations, shown in Fig. 4. As was the case for the F_2 measurements, there is no need in the evolution equations for $(\ln \frac{1}{x})^n$ terms in order to describe the logarithmic slope in x of F_2 .

Even more interesting is the study of $dF_2/d \ln Q^2$. At small x , this derivative is dominated by the convolution of the splitting function P_{qg} and the gluon density, $dF_2/d \ln Q^2 \sim \alpha_S P_{qg} \otimes xg$. As a consequence, xg can be directly related to the measured values of $dF_2/d \ln Q^2$ ¹⁴⁾. The logarithmic slope $dF_2/d \ln Q^2$ has been calculated using the ZEUS data by fitting $F_2 = a + b \ln Q^2$ in bins of fixed x . The results¹³⁾ are shown in Fig. 5. For values of x down to 3×10^{-4} , the slopes increase as x decreases, while at smaller values of x and Q^2 the slopes decrease. It should be noted that each point in Fig. 5 corresponds to a different average value

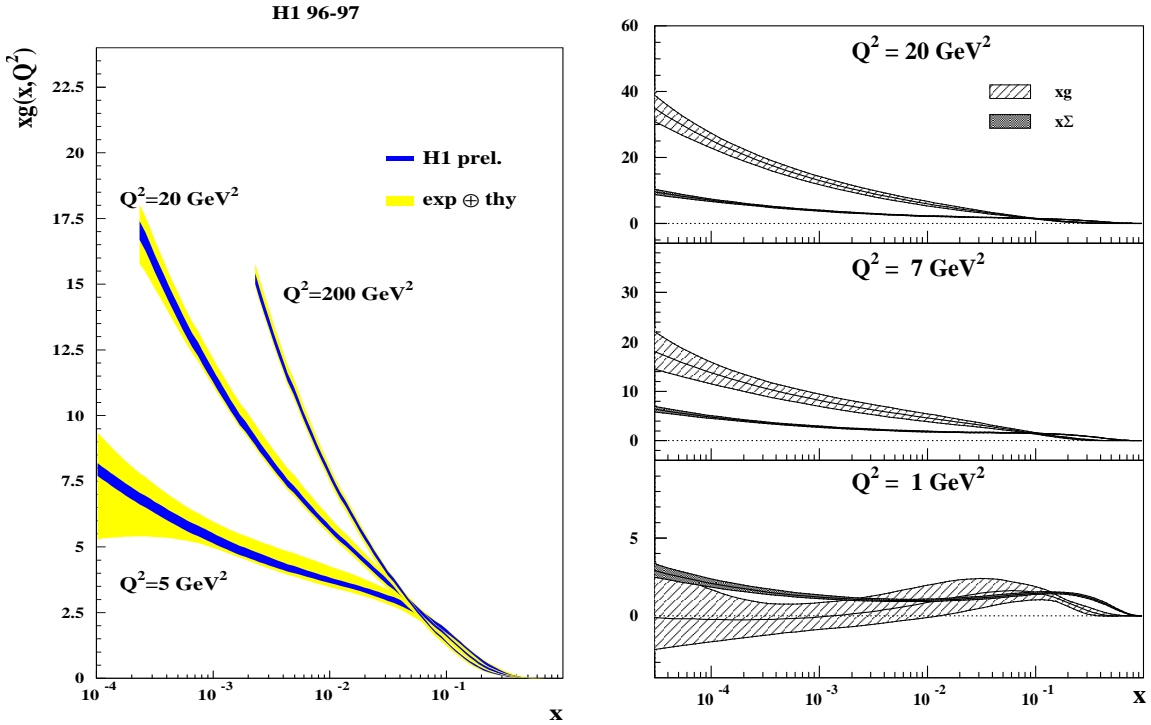


Figure 6: The momentum distributions of partons as obtained by the H1 and ZEUS collaborations. Right: the gluon momentum distribution xg as a function of x at fixed values of $Q^2 = 5, 20$ and 200 GeV^2 from the H1 QCD fit. Left: the quark singlet momentum distribution, $x\Sigma$ (shaded), and the gluon momentum distribution, xg (hatched), as functions of x at fixed values of $Q^2 = 1, 7$ and 20 GeV^2 from the ZEUS QCD fit.

of Q^2 , as indicated at the top of Fig. 5. As predicted by pQCD, the ‘turn over’ is not seen if $dF_2/d\ln Q^2$ is plotted at a fixed value of Q^2 , neither in the fixed target data at $Q^2 > 0.5 \text{ GeV}^2$ ¹⁵⁾ nor in the HERA data at $Q^2 > 3 \text{ GeV}^2$ ⁷⁾. Although the ‘turn over’ is partly a kinematic effect due to averaging over a Q^2 range which is different for different x values, it reflects a smaller rise of the derivatives¹⁶⁾ (i.e. of the gluon density) for $x \rightarrow 0$ when Q^2 decreases below few GeV^2 . We will return to this discussion in the next Section.

3.2.3 The pQCD NLO fits: the gluon and quark singlet momentum densities

In order to extract the parton momentum distributions in the proton, both the H1 and ZEUS collaborations performed a pQCD fit to the F_2 data, solving the DGLAP evolution equations⁹⁾ at NLO in the \overline{MS} renormalisation scheme. In both fits, $\alpha_s(M_{Z^0}) = 0.118$, the momentum sum rule was applied and three light flavours were

considered, the c and b quarks being generated dynamically through boson-gluon fusion (BGF). The H1 fit ⁷⁾ used H1 and NMC data at $3.5 < Q^2 < 3000 \text{ GeV}^2$, while the ZEUS fit ¹³⁾ used ZEUS, NMC and BCDMS data at $1 < Q^2 < 5000 \text{ GeV}^2$. The results for the gluon momentum distribution $xg(x, Q^2)$ vs. x are shown in Fig. 6 at fixed values of Q^2 . Both collaborations measure a strong rise of xg for $x \rightarrow 0$ for $Q^2 \gtrsim 5 \text{ GeV}^2$, with the rise increasing with increasing Q^2 . In Fig. 6 right, the xg obtained by ZEUS is compared to the quark singlet momentum distribution $x\Sigma(x, Q^2) = \sum_{f=u,d,s}[xq_f(x, Q^2) + x\bar{q}_f(x, Q^2)]$ obtained with the same fit. At $Q^2 = 1 \text{ GeV}^2$, the sea is still rising at the lowest x , while the gluon, within large uncertainties, is rising much less and is compatible with zero. These results are not compatible with the assumption that the rise of F_2 at $Q^2 \simeq 1 \text{ GeV}^2$ is entirely driven by the increase of the gluon density at small x due to parton splitting.

3.3 Determination of the longitudinal structure function F_L at small x

The longitudinal structure function F_L is predicted by pQCD to be a function of F_2 and xg (see Eq. 2) and it is expected to give a sizable contribution to the cross section at large values of y . Therefore a measurement of F_L constitutes an important constraint to the theory. In the measurements of F_2 described above, F_L was assumed to be equal to the QCD prediction. A direct measurement ¹⁷⁾ of F_L requires either running the HERA collider at different centre-of-mass energies or using events with initial state QED radiation. The H1 collaboration extracted F_L from the NC cross section measurements using the “subtraction” method ¹⁸⁾. For $Q^2 \ll M_{Z^0}^2$ and neglecting radiative corrections, the NC cross section (1) can be written:

$$\frac{d^2\sigma_{NC}^{ep}}{dx dQ^2} = \frac{2\pi\alpha^2}{xQ^4} Y_+ \cdot \sigma_r$$

where the reduced cross section $\sigma_r = F_2 - (y^2/Y_+) \cdot F_L$. Therefore, at large y , $\sigma_r \simeq F_2 - F_L$ and F_L may be approximated by $F_2 - \sigma_r$. The method used by H1 consists in the subtraction of σ_r from F_2^{QCD} , i.e. the result of the NLO pQCD fit to the 1996-97 F_2 data at $y < 0.35$, for which $F_L \simeq 0$. The results ⁷⁾ obtained with this method for $Q^2 > 10 \text{ GeV}^2$ are shown in Fig. 7. They rely on the extrapolation of F_2^{QCD} beyond $y = 0.35$. In the same Figure the results obtained with another method, which relies on assumptions on the behaviour of the derivative $dF_2/d\ln y$ for $Q^2 < 10 \text{ GeV}^2$, are also shown. The extracted F_L is consistent with the QCD prediction.

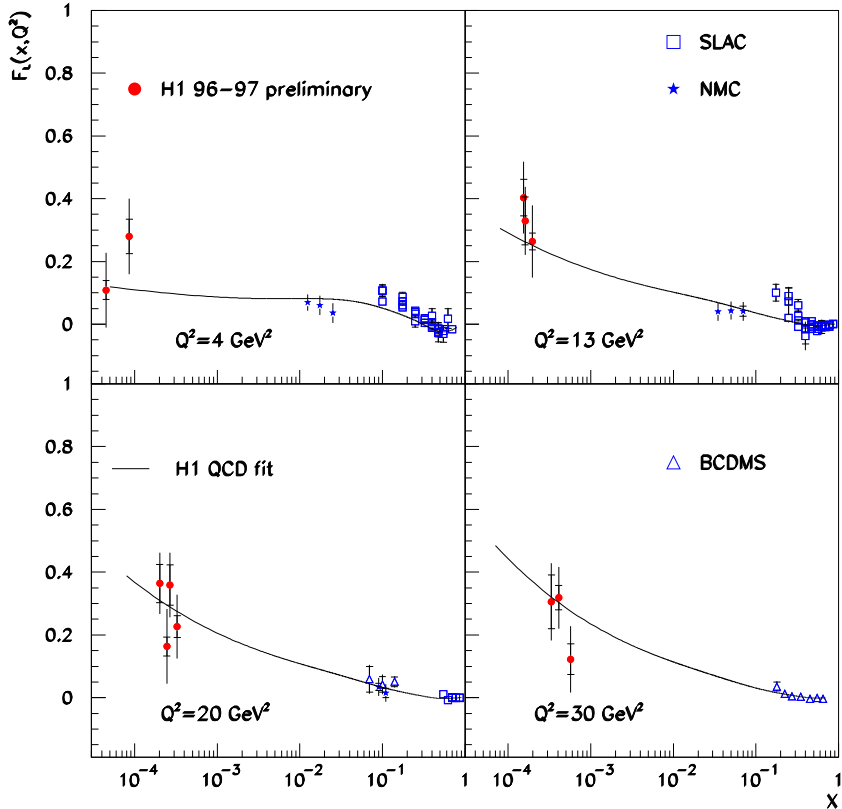


Figure 7: The longitudinal structure function F_L vs. x at fixed Q^2 values. H1, SLAC and NMC data are displayed. The lines represent the H1 NLO pQCD fit results.

3.4 Measurement of the charm structure function $F_2^{c\bar{c}}$

Charm production at HERA is expected to be dominated by BGF¹⁹⁾, i.e. by the gluon density. Therefore, given the large xg measured at HERA for $x \rightarrow 0$ in most of the Q^2 range, we expect the charm contribution to F_2 to be large. In analogy with Eq. (1), for not too large Q^2 and y and neglecting radiative corrections, the charm structure function $F_2^{c\bar{c}}$ is defined as:

$$\frac{d^2\sigma^{c\bar{c}}}{dx dQ^2} = \frac{2\pi\alpha^2}{xQ^4} Y_+ F_2^{c\bar{c}}(x, Q^2).$$

Experimentally, the cross section for the production of a $c\bar{c}$ pair, $\sigma^{c\bar{c}}$, is extracted from the visible cross section for the production of D^* mesons, σ^{D^*} , after correction for the $c \rightarrow D^*$ fragmentation and extrapolation to the full (η, p_T) range. This measurement is a very effective test of QCD, since $F_2^{c\bar{c}}$ is also calculable from pQCD knowing xg from the F_2 scaling violations and applying the BGF NLO calculations¹⁹⁾. The result of such a calculation can be compared to the direct measure-

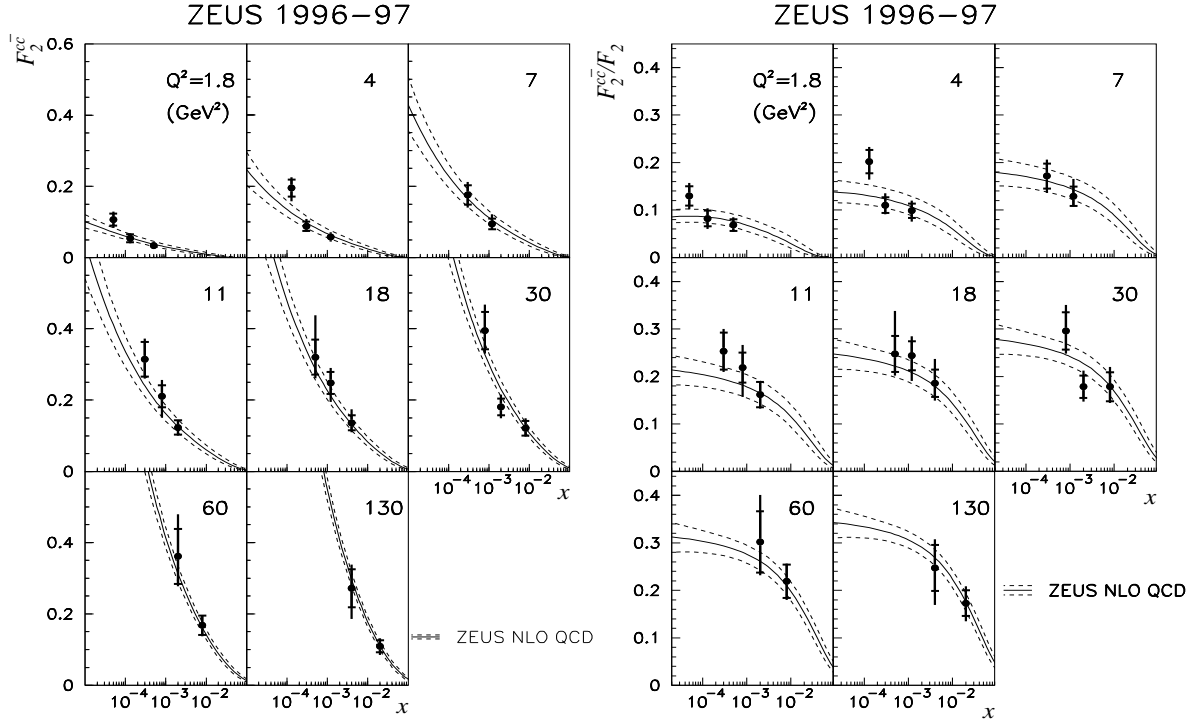


Figure 8: Measurement of $F_2^{c\bar{c}}$ (left) and $F_2^{c\bar{c}}/F_2$ (right) vs. x in bins of Q^2 . The full lines are the result of the ZEUS pQCD NLO fit, while the dashed lines represent the uncertainty of the fit, dominated by the variation by 0.2 MeV of the charm mass around the central value $m_c = 1.4$ GeV.

ment of $F_2^{c\bar{c}}$. Fig. 8 left, shows the ZEUS measurement²⁰⁾ of $F_2^{c\bar{c}}$ vs. x in bins of Q^2 . A steep rise of $F_2^{c\bar{c}}$ is measured for $x \rightarrow 0$, the rise being more pronounced at large Q^2 . The NLO QCD fit is in agreement with the data, which proves that the BGF diagram is the dominant mechanism for charm production at HERA. The ratio $F_2^{c\bar{c}}/F_2$ is shown in Fig. 8 right. For $x \rightarrow 0$, $F_2^{c\bar{c}}$ rises more rapidly than F_2 , is ~ 25 % of F_2 at low x and high Q^2 and decreases to 10 % at $Q^2 = 1.8$ GeV 2 . Since $F_2^{c\bar{c}}$ is dominated by the gluon contribution while F_2 contains also the sea quarks, the $F_2^{c\bar{c}}/F_2$ behaviour¹ is consistent with the hypothesis that the ratio $gluons/(gluons + sea)$ decreases for $Q^2 \rightarrow 0$, as has been shown in Sections 3.2.2 and 3.2.3.

4 $e^\pm p$ cross sections at large Q^2

¹The effect of the charm-mass threshold is negligible at the small x values discussed here²¹⁾

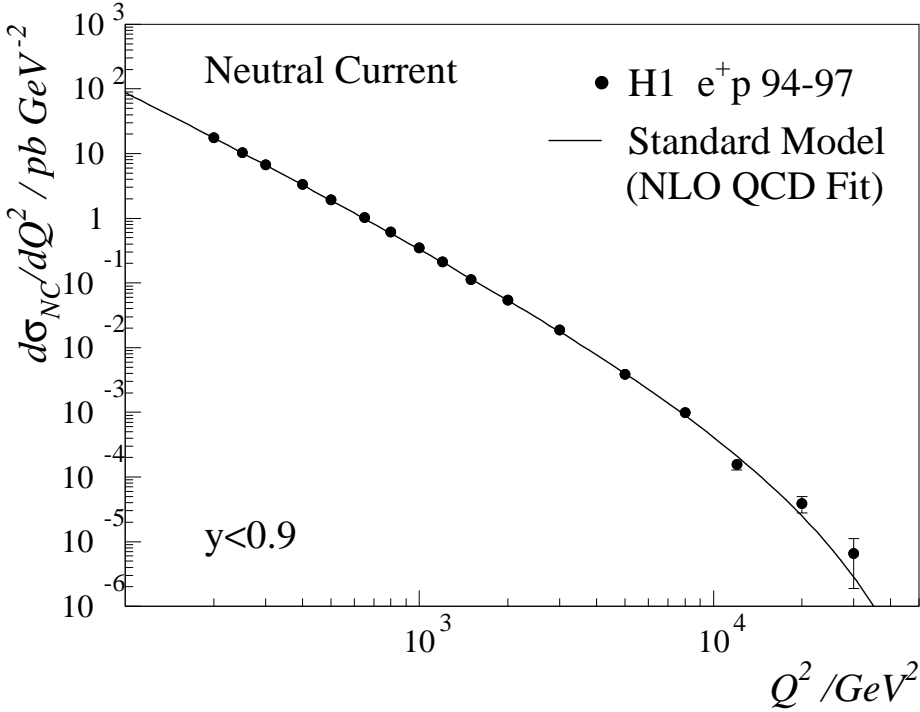


Figure 9: The $d\sigma_{NC}/dQ^2$ for e^+p scattering at HERA. The line represents the Standard Model prediction described in the text.

4.1 Neutral currents

For Q^2 beyond a few thousand GeV^2 , the parity violating structure function xF_3 becomes sizable and can no longer be neglected. In this case we will write the NC cross section:

$$\frac{d^2\sigma_{NC}^{e^\pm p}}{dx dQ^2} = \frac{2\pi\alpha^2}{xQ^4} [Y_+\tilde{F}_2(x, Q^2) \mp Y_-x\tilde{F}_3(x, Q^2)] \quad (3)$$

having neglected radiative corrections and F_L . The structure functions themselves contain contributions from virtual photon and Z^0 exchange:

$$\begin{aligned} \tilde{F}_2 &= F_2^{em} + \frac{Q^2}{(Q^2 + M_{Z^0}^2)} F_2^{int} + \frac{Q^4}{(Q^2 + M_{Z^0}^2)^2} F_2^{wk} \\ \tilde{F}_3 &= \frac{Q^2}{(Q^2 + M_{Z^0}^2)} F_3^{int} + \frac{Q^4}{(Q^2 + M_{Z^0}^2)^2} F_3^{wk} \end{aligned}$$

where the superscripts em , wk and int indicate the contributions due to photon exchange, Z^0 exchange and γZ^0 interference. The measured ²²⁾ e^+p NC cross section vs. Q^2 is shown in Fig. 9. The fall of $d\sigma_{NC}^{e^\pm p}/dQ^2$ over seven orders of magnitude constitutes a great success for the Standard Model. The extrapolation to large Q^2 values of the NLO pQCD fit, including the EW propagator terms, obtained

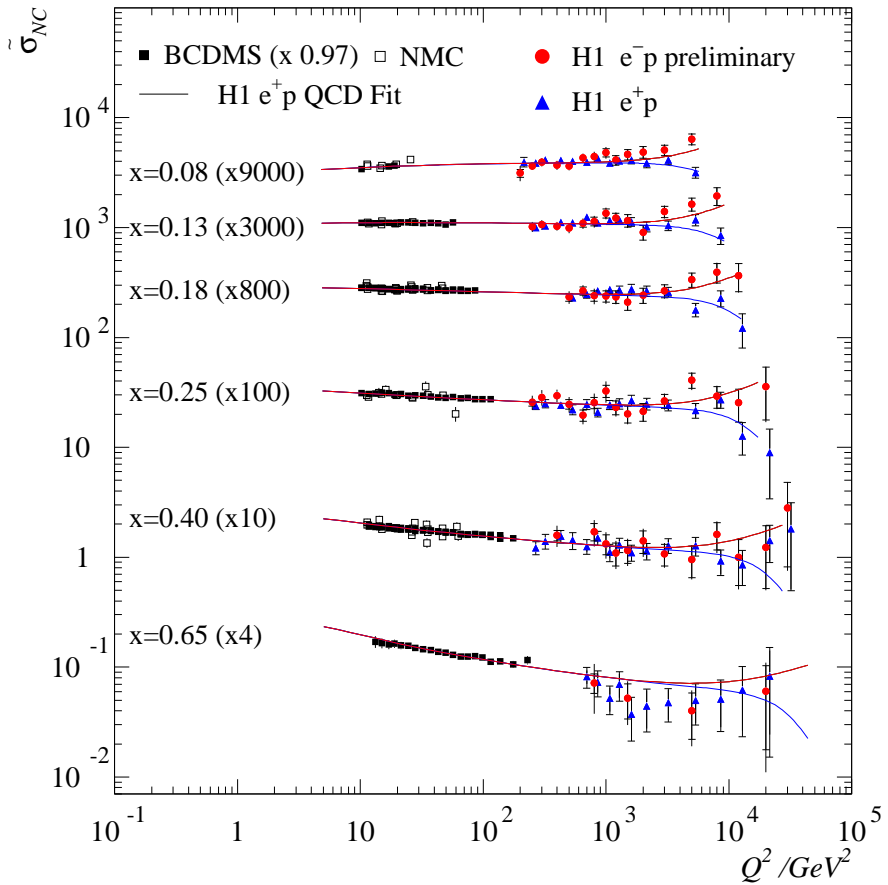


Figure 10: The reduced cross section $\tilde{\sigma}_{NC}$ for e^+p and e^-p collisions. The effect of the γZ^0 interference is evident at the largest Q^2 and is in agreement with the theory.

with the data at $Q^2 < 120$ GeV 2 describes the data well, proving the validity of the theory in such a wide Q^2 range. Larger luminosities are needed to constrain the PDFs at the largest (x, Q^2) values.

The structure function xF_3 enters in Eq. (3) with a $-$ or $+$ sign depending if the lepton beam consists of positrons or electrons, respectively. Therefore the collection of both e^-p and e^+p data samples permit a measurement of xF_3 . The reduced cross section:

$$\tilde{\sigma}_{NC} = Y_+ \tilde{F}_2(x, Q^2) \mp Y_- x \tilde{F}_3(x, Q^2)$$

is shown in Fig. 10 for both e^+p and e^-p data ²³⁾. For $Q^2 > 3000$ GeV 2 , the e^-p cross sections are larger than the e^+p ones, as expected from the Standard Model γZ^0 interference.

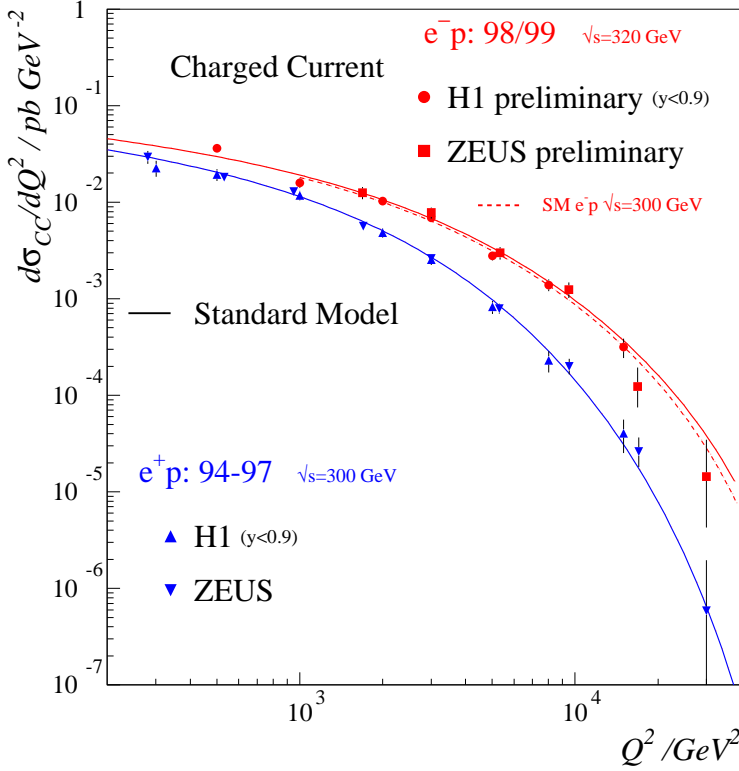


Figure 11: *HERA CC differential cross sections vs. Q^2 for e^+p and e^-p scattering.* The HERA 1994-97 data at $\sqrt{s} = 300$ GeV and the 1998-99 data at $\sqrt{s} = 318$ GeV are plotted. The lines represent the Standard Model predictions.

4.2 Charged currents

The charged current (CC) double-differential cross section can be written:

$$\frac{d^2\sigma_{CC}^{e^\pm p}}{dx dQ^2} = \frac{G_F^2}{2\pi x} \cdot \left[\frac{M_W^2}{Q^2 + M_W^2} \right]^2 \cdot \Phi_{CC}^\pm(x, Q^2) \quad (4)$$

where G_F is the Fermi constant and M_W is the W^\pm boson mass. In the naive quark-parton model:

$$\Phi_{CC}^+(x, Q^2) = \bar{u} + (1 - y)^2 \cdot (d + s)$$

$$\Phi_{CC}^-(x, Q^2) = u + (1 - y)^2 \cdot (\bar{d} + \bar{s}).$$

It should be noticed that in the case of e^-p scattering the CC cross section is directly sensitive to quarks (whereas $\sigma_{CC}^{e^+p}$ is sensitive to antiquarks) and that in the case of e^+p scattering the helicity factor $(1 - y)^2$ multiplies the quark densities. For both these reasons we expect $\sigma_{CC}^{e^-p} > \sigma_{CC}^{e^+p}$ at large (x, Q^2) , where valence quarks must dominate. Fig. 10 shows the HERA CC differential cross sections [23, 24, 25, 26] as

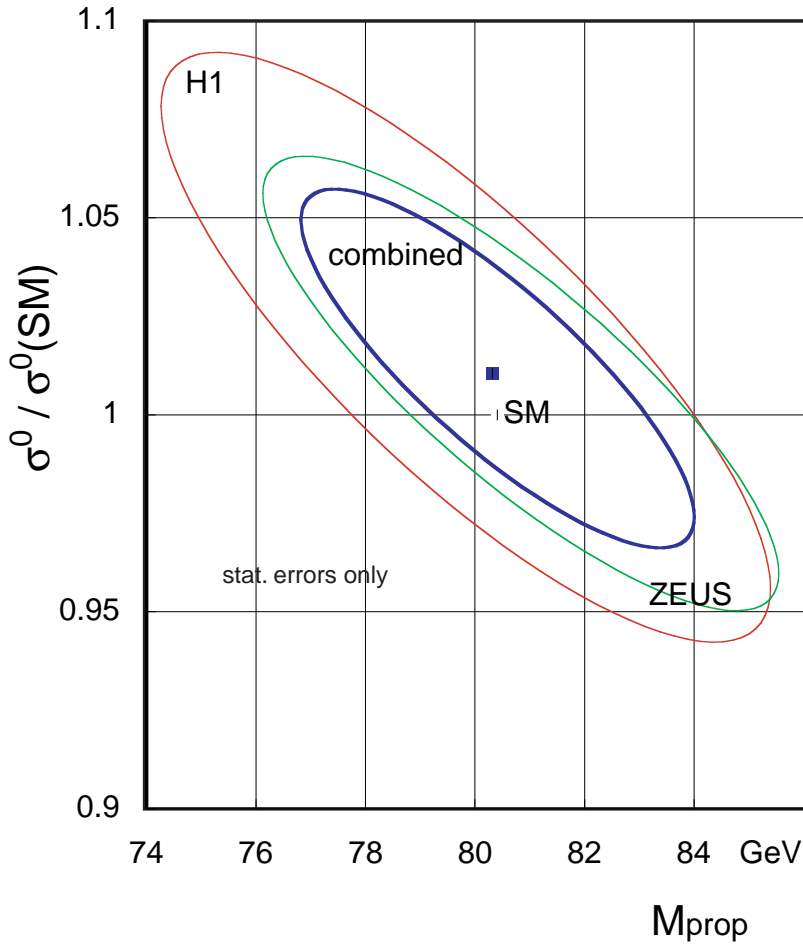


Figure 12: The HERA measurements of the CC cross section with respect to the Standard Model, $\sigma^0/\sigma^0(\text{SM}) \propto G_F$, and of the W -propagator mass. The one sigma contours are obtained using only the statistical uncertainties.

a function of Q^2 , both for e^+p and e^-p scattering. The difference between $\sigma_{CC}^{e^-p}$ and $\sigma_{CC}^{e^+p}$ increases with Q^2 , reaching approximately one order of magnitude at $Q^2 \simeq 10^4$ GeV 2 . The Standard Model describes the data well.

4.2.1 Measurements of the W -propagator mass

Charged current reactions are mediated by the exchange of a virtual W^\pm . It is important to measure the W -propagator mass, i.e. the mass of a *spacelike* W , since a deviation from the *timelike-W* mass measured in e^+e^- and pp collisions may reveal an anomalous spacelike EW sector. In Eq. (4) the absolute magnitude of the cross section is given by G_F and the functions Φ^\pm , while the cross-section shape is entirely contained in the propagator term. The H1 and ZEUS collaborations fitted the CC

cross section with two free parameters, the coupling G_F and the propagator mass M_W . The results are shown in Fig. 11, where the H1 and ZEUS one sigma contour distributions, and the combined one, are given. Both collaborations find ^{24, 25)} the W -propagator mass in agreement with the timelike- W mass within a statistical uncertainty of approximately 5 GeV. This result proves the universality of the CC interactions over a wide range of Q^2 . The fit has been repeated constraining the cross-section normalisation using the precise value $G_F = (1.16639 \pm 0.00001) \cdot 10^{-5}$ GeV², measured in muon decay. In this case, the results are in agreement with the timelike- W mass within ~ 3 GeV (*stat.*) and ~ 5 GeV (*stat. \oplus syst.*). Finally, to exploit the strong dependence of the cross-section normalisation (G_F) on the shape (M_W) in a model-dependent fit, ZEUS used the Standard Model relation:

$$G_F = \frac{\pi\alpha}{\sqrt{2}} \cdot \frac{M_{Z^0}^2}{M_W^2(M_{Z^0}^2 - M_W^2)} \cdot \frac{1}{1 - \Delta r(M_W)}$$

where $\Delta r(M_W)$ contains the radiative corrections to the lowest-order expression for G_F and is a function of α and the masses of the fundamental bosons and fermions. Using this relation, the 3% cross-section uncertainty is cast in the uncertainty of a single EW parameter, and the uncertainty on the W -propagator mass is expected to reduce by a large factor. The result of this model-dependent fit is ²⁵⁾:

$$M_W = 80.50^{+0.24}_{-0.25}(\textit{stat.})^{+0.13}_{-0.16}(\textit{syst.}) \pm 0.31(\textit{PDF})^{+0.03}_{-0.06}(\Delta M_t, \Delta M_H, \Delta M_Z) \text{GeV.}$$

where the last uncertainty is obtained by varying the masses of the top quark, the Higgs and the Z^0 bosons.

4.3 Comparison of NC and CC cross sections

The Standard Model predicts that, with increasing Q^2 , NC and CC should become of equal magnitude. This prediction can be verified at HERA, given the large range in Q^2 . Fig. 13 shows the ZEUS and H1 measurements of the differential e^-p NC and CC cross sections as a function of Q^2 . At $Q^2 \simeq 10^4$ GeV² the e^-p NC and CC cross sections reach similar values. The Standard Model predictions are in good agreement with the measurements. We conclude that the unification of charged currents and neutral currents has been verified at HERA.

5 Summary and outlook

The study of structure functions at HERA has reached a mature stage. The structure function F_2 has been measured in a very wide kinematic range, $10^{-1} < Q^2 < 10^5$

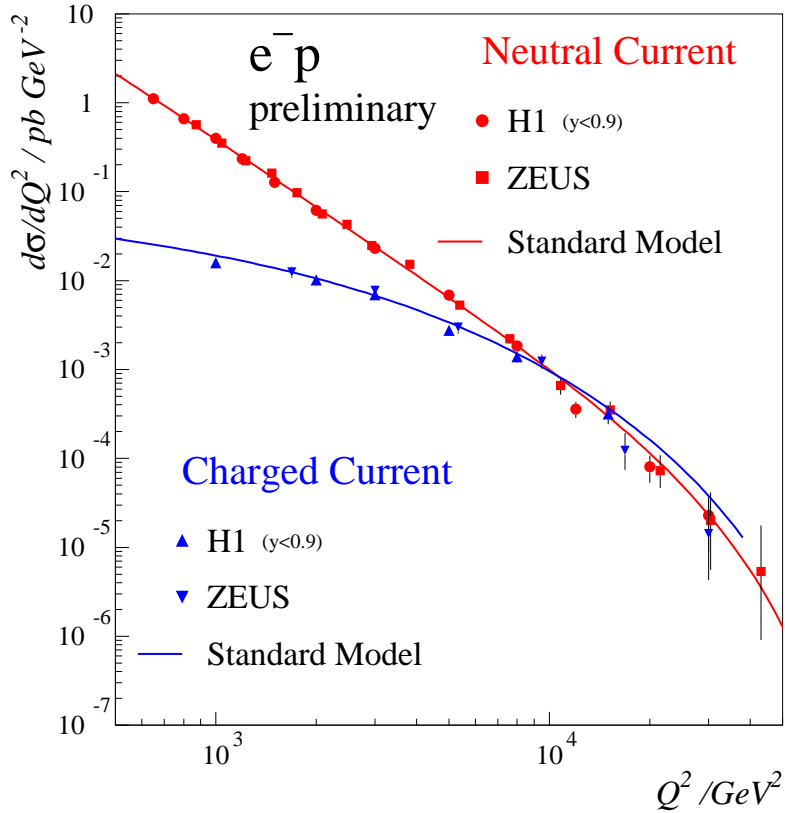


Figure 13: The HERA measurements of NC and CC $e^- p$ cross sections, showing their unification at large Q^2 , as predicted by the Standard Model.

GeV^2 and x down to 10^{-6} . Precisions of a few percent have been reached in a large fraction of the above range. At the lowest Q^2 measured, F_2 can be described by Regge phenomenology. For Q^2 above few GeV^2 , the region where pQCD is expected to be applicable, the DGLAP evolution works well and no need is found for the BFKL $(\ln \frac{1}{x})^n$ correction terms. In this region F_2 rises strongly towards small x ; hints have been found that at small Q^2 this rise may be driven by sea quarks, and not by gluons. The charm structure function $F_2^{c\bar{c}}$ is measured to be a substantial contribution to F_2 , reaching 25% at small x and large Q^2 . Indirect determinations of the longitudinal structure function F_L agree with the QCD expectation.

The first measurements of the NC and CC cross sections at very large Q^2 have been made in $e^\pm p$ scattering. The Standard Model predictions agree with the data. In NC interactions, γZ^0 interference has been observed, while in CC interactions the W -propagator mass has been measured to be consistent with the timelike- W mass within a few GeV. The unification of NC and CC interactions at very large Q^2 has been measured in $e^- p$ scattering.

Overall, the Standard Model is found to be in good agreement with the measurements based on approximately 100 pb^{-1} of data collected at HERA by each collider experiment. The plans for the future are to increase the integrated luminosity by an order of magnitude. In Summer 2000 HERA will be shut down for nine months. During this period, superconducting magnets will be installed inside the H1 and ZEUS detectors to achieve stronger beam focusing at the interaction points and obtain an increase of a factor of five in specific luminosity. The plans are to run for at least five more years to integrate $\sim 1\text{ fb}^{-1}$ of data, which will give full access to the electroweak physics programme and to the search for physics beyond the Standard Model at HERA.

6 Acknowledgements

I wish to thank the organisers of the workshop for providing once again the optimal conditions to enjoy life and physics at the same time. I am indebted to the many ZEUS and H1 colleagues from which I have learned much. I particularly thank Brian Foster for carefully reading and commenting on the manuscript and Jack Smith for elucidating theoretical aspects of charm production at HERA.

References

1. R. Gandhi *et al.*, Phys. Rev. **D 58**, 093009 (1998);
J. Kwiecinski *et al.*, hep-ph/0004109.
2. A.M. Cooper-Sarkar *et al.*, Int. J. Mod. Phys. **A13**, 3385 (1988), and ref. therein.
3. L.V. Gribov *et al.*, Phys. Rep. **100**, 1 (1983).
4. V.S. Fadin *et al.*, Phys. Lett. **B422**, 287 (1998);
G. Altarelli *et al.*, hep-ph/0001157 and ref. therein.
5. R. Cashmore *et al.*, Proc. of the DESY workshop on Future Physics at HERA, ed. G. Ingelman *et al.*, 127 (1996), <http://www.desy.de/~heraws96>.
6. ZEUS Collab., J. Breitweg *et al.*, DESY 00-071 (May 2000), submitted to Phys. Lett. B.
7. Max Klein, Talk given at the XIX International Symposium on Lepton and Photon Interactions at High Energies, Stanford, August 1999, hep-ex/0001059.
8. Niels Tuning, Talk given at the DIS2000 Workshop on DIS, Liverpool, April 2000.

9. G. Altarelli and G. Parisi, Nucl. Phys. **B126**, 298 (1977);
 V. Gribov and L. Lipatov, Sov. Jour. Nucl. Phys. **15**, 438 (1972);
 L. Lipatov, Sov. Jour. Nucl. Phys. **20**, 94 (1975);
 Y. Dokshitzer, Sov. Phys. JETP **46**, 641 (1977).
10. J. Bartels *et al.*, Proc. of the DESY Workshop Physics at HERA, ed. W. Buchmüller and G. Ingelman, 193 (1991).
11. H. Navelet, R. Peschanski and S. Wallon, Mod. Phys. Lett **A36**, 3393 (1994).
12. H. Navelet et al., Phys. Lett. **B385** (1996) 357.
13. ZEUS Collab., J. Breitweg *et al.*, Eur. Phys. J. **C7**, 609 (1999).
14. K. Prytz, Phys. Lett. **B311**, 286 (1993); *ibid* **B 332**, 393 (1994).
15. A.D. Martin *et al.*, Eur. Phys. J. **C4**, 463 (1998).
16. K. Golec-Biernat and M. Wünnsthoff, Phys. Rev. **D60**, 114023 (1999) and ref. therein.
17. L.A.T. Bauerdic *et al.*, Proc. of the DESY workshop on Future Physics at HERA, ed. G. Ingelman *et al.*, 77 (1996), <http://www.desy.de/~heraws96>.
18. H1 Collab., C. Adloff *et al.*, Phys. Lett. **B393**, 452 (1997).
19. B.W. Harris and J. Smith, Phys. Rev. **D57**, 2806 (1998).
20. ZEUS Collab., J. Breitweg *et al.*, Eur. Phys. J **C12**, 35 (2000).
21. Jack Smith, Proc. of the Workshop New Trends in HERA Physics, Ringberg, May 1997, hep-ph/9708212.
22. H1 Collab., C. Adloff *et al.*, Eur. Phys. J. **C13**, 609 (2000),
 ZEUS Collab., J. Breitweg *et al.*, Eur. Phys. J. **C11** 3, 427 (1999).
23. H1 Collab., C. Adloff *et al.*, contribution n. 157b, EPS99, Tampere, Finland, July 1999.
24. H1 Collab., C. Adloff *et al.*, contribution n. 157ai, EPS99, Tampere, Finland, July 1999.
25. ZEUS Collab., J. Breitweg *et al.*, Eur. Phys. J. **C12** 3, 411 (2000).
26. ZEUS Collab., J. Breitweg *et al.*, contribution n. 558, EPS99, Tampere, Finland, July 1999.